remote sensing

MDPI

Technical Note

A New Probability Distribution for SAR Image Modeling

Murilo Sagrillo [1,*,†], Renata R. Guerra [2,†], Fábio M. Bayer [3] and Renato Machado [4]

[1] Programa de Pós-Graduação em Engenharia de Produção, Universidade Federal de Santa Maria, Santa Maria 97105-900, Brazil
[2] Departamento de Estatística, Universidade Federal de Santa Maria, Santa Maria 97105-900, Brazil; renata.r.guerra@ufsm.br
[3] Departamento de Estatística and LACESM, Universidade Federal de Santa Maria, Santa Maria 97105-900, Brazil; bayer@ufsm.br
[4] Department of Telecommunications, Aeronautics Institute of Technology (ITA), São José dos Campos 12228-900, Brazil; rmachado@ita.br
* Correspondence: murilo.pereira@acad.ufsm.br
† These authors contributed equally to this work.

Abstract: This article introduces exponentiated transmuted-inverted beta (ET-IB) distribution, supported by a continuous positive real line, as a synthetic aperture radar (SAR) imagery descriptor. It is an extension of the inverted beta distribution, an important texture model for SAR imagery. The considered distribution extension approach increases the flexibility of the baseline distribution, and is a new probabilistic model useful in SAR image applications. Besides introducing the new model, the maximum likelihood method is discussed for parameter estimation. Numerical experiments are performed to validate the use of the ET-IB distribution as a SAR amplitude image descriptor. Finally, three measured SAR images referring to forest, ocean, and urban regions are considered, and the performance of the proposed distribution is compared to distributions usually considered in this field. The proposed distribution outperforms the competitor models for modeling SAR images in terms of some selected goodness-of-fit measures. The results show that the ET-IB distribution is suitable as a SAR descriptor and can be used to develop image-processing tools in remote sensing applications.

Keywords: beta prime distribution; exponentiated transmuted-inverted beta model; probability distribution; SAR image; statistical models

check for updates

Citation: Sagrillo, M.; Guerra, R.R.; Bayer, F.M.; Machado, R. A New Probability Distribution for SAR Image Modeling. *Remote Sens.* **2022**, *14*, 2853. https://doi.org/10.3390/rs14122853

Academic Editor: John Trinder

Received: 6 May 2022
Accepted: 6 June 2022
Published: 14 June 2022

Publisher's Note: MDPI stays neutral with regard to jurisdictional claims in published maps and institutional affiliations.

Copyright: © 2022 by the authors. Licensee MDPI, Basel, Switzerland. This article is an open access article distributed under the terms and conditions of the Creative Commons Attribution (CC BY) license (https://creativecommons.org/licenses/by/4.0/).

1. Introduction

Statistical modeling provides technical support for synthetic aperture radar (SAR) image processing and interpretation, allowing a better understanding of the terrain scattering mechanism [1]. It is also a recurring topic in radar-signal-processing applications such as edge detection [2], land cover classification [3], and target detection [4].

Depending on the SAR system characteristics, such as bandwidth, central frequency, pulse format, number of looks for generating the final image, and scene under observation, certain distributions can be more suitable for modeling it [1]. The Rayleigh and Weibull distributions are commonly used for modeling amplitude in single-look SAR images [1], and the exponential and Weibull are typical choices for fitting intensity in single-look images [1,5]. Additionally, the gamma, inverse gamma, $\mathcal{G}_A^0$, and $\mathcal{G}_I^0$ distributions are well-known options for multi-look images [1]. However, to add flexibility and improve the goodness-of-fit for different settings of SAR image data, some flexible alternatives of probability distributions have been proposed in the literature (see, for instance, [6–11]), and are shown to be a practice of great relevance in the area.

In this sense, the goals of this paper are twofold. First, we introduce a four-parameter distribution as a SAR image descriptor. With the name of exponentiated transmuted inverted beta (ET-IB) distribution, the new model is obtained by extending the inverted beta (IB) distribution [12]. Known as beta prime, or beta distribution of the second kind, the

IB distribution has been considered as a texture model for SAR image applications [13,14]. Our proposal generalizes the IB distribution from the exponentiated transmuted-G (ET-G) class [15]. The ET-G framework introduces two shape parameters in an existing distribution (baseline) to make it more flexible, especially for fitting asymmetric and heavy-tailed data. To the best of our knowledge, only a few studies generalize specific baselines on the ET-G family. For example, we can refer to Okereke [16] for the exponentiated transmuted Lindley distribution and Abbas et al. [17], who introduced the exponentiated transmuted length-biased exponential distribution. However, neither of them explored possible applications in SAR image modeling. Second, we show the suitability of the ET-IB distribution as a SAR descriptor by using simulated and measured amplitude images. The analysis focus on images related to forest, ocean, and urban regions. Moreover, the new model could be used for many applications, such as deforestation monitoring, crop growth, biomass quantification, military activity surveillance, maritime surveillance, oil slick detection, ship detection, search and rescue, and illegal activities monitoring [18–21]. In fact, the proposed ET-IB model can replace the IB distribution in any algorithm where it is appropriate. It is possible to improve the overall performance of the algorithm once the process of generalizing distributions tends to enhance the flexibility and goodness-of-fit of the baseline distribution. Using real SAR data, we compare the goodness-of-fit of the ET-IB distribution with its baseline and several classical statistical models for amplitude in SAR image interpretation. The results show that the proposed ET-IB distribution outperforms the competitor models.

Considering the above discussion, we summarize the contributions of the paper as follows:

- A new probability model is proposed, which is an extension of an important texture model of SAR imagery;
- The maximum likelihood theory is developed for parameter estimation;
- Numerical experiments with synthetic signals are performed to validate the proposed model and inference theory;
- Based on three measured SAR images, we show that the proposed model outperforms several well-known SAR image descriptors;
- A collection of computational codes are available to guarantee reproducibility of the results and future applications of the proposal.

The rest of this paper is organized as follows. In Section 2, we present statistical preliminaries on the ET-G family and IB distribution, derive the proposed ET-IB distribution as a novel statistical tool for SAR image modeling, and discuss parameter estimation. Section 3 presents some possible applications for the ET-IB distribution. Finally, Section 4 provides conclusions and final remarks.

2. The Exponentiated Transmuted Inverted Beta Distribution

This section provides the necessary statistical background for understanding the derivation of the proposed ET-IB distribution.

2.1. Statistical Preliminaries

The random variable X with IB distribution has a probability density function (pdf) and a cumulative distribution function (cdf) that are given by [12]

$$g_X(x;\alpha,\beta) = \frac{x^{\alpha-1}(1+x)^{-\alpha-\beta}}{B(\alpha,\beta)}, \quad x>0, \tag{1}$$

and

$$G_X(x;\alpha,\beta) = I_{x/(1+x)}(\alpha,\beta) = \frac{B(x/(1+x),\alpha,\beta)}{B(\alpha,\beta)}, \tag{2}$$

respectively, where $\alpha, \beta > 0$, $\mathrm{B}(a,b) = \Gamma(a)\Gamma(b)/\Gamma(a+b)$ is the beta function, and $\Gamma(\cdot)$ is the gamma function. The beta and gamma functions are both efficiently implemented in several programming languages. $\mathrm{I}_z(a,b)$ is the regularized incomplete beta function, and $\mathrm{B}(z,a,b) = \int_0^z t^{a-1}(1-t)^{b-1}\mathrm{d}t$ is the incomplete beta function. The parameters α and β control the shape and skewness of the IB distribution [22].

The ET-G family of continuous distributions was proposed to increase the flexibility of a baseline distribution [15]. The cdf and pdf for continuous ET-G distributions are given by

$$\mathrm{F}_X(x;\phi,\lambda,\boldsymbol{\zeta}) = \mathrm{G}_X(x;\boldsymbol{\zeta})^{\phi}[1+\lambda-\lambda\mathrm{G}_X(x;\boldsymbol{\zeta})]^{\phi}, \tag{3}$$

and

$$\mathrm{f}_X(x;\phi,\lambda,\boldsymbol{\zeta}) = \phi \mathrm{g}_X(x;\boldsymbol{\zeta})[1+\lambda-2\lambda\mathrm{G}_X(x;\boldsymbol{\zeta})]\mathrm{G}_X(x;\boldsymbol{\zeta})^{\phi-1}[1+\lambda-\lambda\mathrm{G}_X(x;\boldsymbol{\zeta})]^{\phi-1},$$

respectively, where $\phi > 0$ and $|\lambda| < 1$ are the additional parameters of the ET-G family and $\boldsymbol{\zeta}$ is the parameter vector of the baseline distribution with cdf $\mathrm{G}_X(x;\boldsymbol{\zeta})$.

2.2. The Model Description

The cdf of the ET-IB is defined by inserting (2) in (3), and is given by

$$\mathrm{F}_X(x;\boldsymbol{\theta}) = \mathrm{I}_{x/(1+x)}(\alpha,\beta)^{\phi}\left[1+\lambda-\lambda\mathrm{I}_{x/(1+x)}(\alpha,\beta)\right]^{\phi}, \tag{4}$$

where $x, \alpha, \beta, \phi > 0$, $|\lambda| < 1$, and $\boldsymbol{\theta} = (\alpha,\beta,\phi,\lambda)^{\top}$ is the parameter vector. The corresponding pdf is

$$\mathrm{f}_X(x;\boldsymbol{\theta}) = \frac{\phi x^{\alpha-1}\mathrm{I}_{x/(1+x)}(\alpha,\beta)^{\phi-1}}{(1+x)^{\alpha+\beta}\mathrm{B}(\alpha,\beta)}\left[1+\lambda-2\lambda\mathrm{I}_{x/(1+x)}(\alpha,\beta)\right]\left[1+\lambda-\lambda\mathrm{I}_{x/(1+x)}(\alpha,\beta)\right]^{\phi-1}. \tag{5}$$

Hereafter, a random variable with density (5) is denoted by $X \sim \text{ET-IB}(\alpha,\beta,\phi,\lambda)$.

Some pdf plots are presented in Figure 1 to illustrate the effect of different parameter combinations in the new probability density function (5). The proposed pdf is suitable for modeling SAR images with asymmetry, positive skewness, heavy tail, and different degrees of variability, giving support to many SAR applications (see [2,4,9]). A shiny application that allows the reader to access dynamical plots with other parameter combinations and density shapes is available in [23].

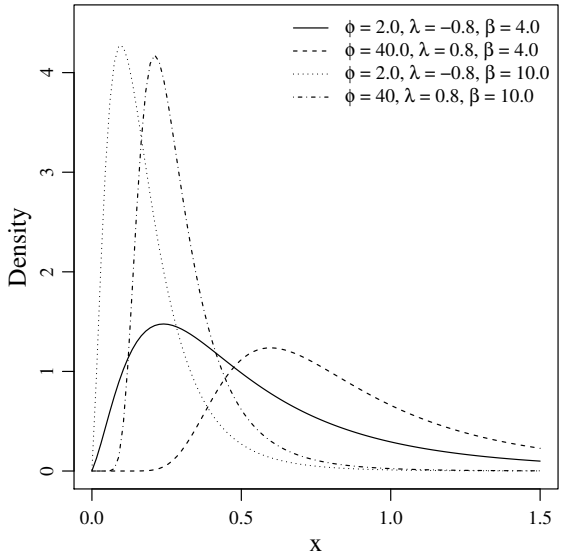


Figure 1. Examples of density formats of the ET-IB distribution for $\alpha = 0.8$.

Finally, by inverting (4), we obtain the quantile function of X, which is given by

$$\mathrm{Q}(u;\boldsymbol{\theta}) = \begin{cases} \left[1-\mathrm{T}\left(\frac{\lambda-\sqrt{(\lambda+1)^2-4\lambda u^{1/\phi}}+1}{2\lambda},\alpha,\beta\right)\right]^{-1}-1, & \text{for } \lambda\neq 0, \\ \left[1-\mathrm{T}\left(u^{1/\phi},\alpha,\beta\right)\right]^{-1}-1, & \text{for } \lambda = 0, \end{cases} \tag{6}$$

where $\mathrm{T}(u,\alpha,\beta)$ is the quantile function of the beta distribution with parameters $\alpha>0$ and $\beta>0$.

Considering the inversion method, if u is an observation of a uniform random variable on the unit interval, we can replace u in (6) to generate random numbers from the ET-IB distribution. Additionally, using (6), we can calculate the Bowley's skewness (S_B) [24] based on quartiles and the Moor's kurtosis (K_M) [25] based on octiles, given by

$$S_B = \frac{\mathrm{Q}(3/4;\boldsymbol{\theta})-2\mathrm{Q}(1/2;\boldsymbol{\theta})+\mathrm{Q}(1/4;\boldsymbol{\theta})}{\mathrm{Q}(3/4;\boldsymbol{\theta})-\mathrm{Q}(1/4;\boldsymbol{\theta})}$$

and

$$K_M = \frac{\mathrm{Q}(7/8;\boldsymbol{\theta})-\mathrm{Q}(5/8;\boldsymbol{\theta})-\mathrm{Q}(3/8;\boldsymbol{\theta})+\mathrm{Q}(1/8;\boldsymbol{\theta})}{\mathrm{Q}(6/8;\boldsymbol{\theta})-\mathrm{Q}(2/8;\boldsymbol{\theta})}.$$

2.3. Likelihood Inference

In practice, the parameters of the ET-IB distribution are usually unknown and need to be estimated. In this study, we consider the maximum likelihood theory for this purpose due to the easy obtainment and good properties, such as consistency and asymptotic efficiency of the maximum likelihood estimator (MLE) (see [26], for more information).

Let $x_1,\ldots,x_n$ be a signal of length n from $X\sim$ ET-IB$(\alpha,\beta,\phi,\lambda)$. The MLE of $\boldsymbol{\theta}$ is given by

$$\hat{\boldsymbol{\theta}} = \underset{\boldsymbol{\theta}\in\boldsymbol{\Theta}}{\arg\max}\,\ell(\boldsymbol{\theta}),$$

where $\hat{\boldsymbol{\theta}}=(\hat{\alpha},\hat{\beta},\hat{\phi},\hat{\lambda})^\top$, $\boldsymbol{\Theta}$ is the parametric space of $\boldsymbol{\theta}$, and

$$\begin{aligned}\ell(\boldsymbol{\theta}) &= \sum_{i=1}^{n}\log(\mathrm{f}_X(\boldsymbol{\theta}|x_i)) = n\log(\phi)+(\alpha-1)\sum_{i=1}^{n}\log(x_i)-(\alpha+\beta)\sum_{i=1}^{n}\log(1+x_i)\\ &+(\phi-1)\sum_{i=1}^{n}\log\left[\mathrm{I}_{x_i/(1+x_i)}(\alpha,\beta)\right]+\sum_{i=1}^{n}\log\left[1+\lambda-2\lambda\mathrm{I}_{x_i/(1+x_i)}(\alpha,\beta)\right]\\ &+(\phi-1)\sum_{i=1}^{n}\log\left[1+\lambda-\lambda\mathrm{I}_{x_i/(1+x_i)}(\alpha,\beta)\right]\end{aligned} \tag{7}$$

is the log-likelihood function of $\boldsymbol{\theta}$ for the observed signal.

Differentiating (7) with respect to each unknown parameter, we obtain the score vector

$$\mathrm{U}(\boldsymbol{\theta}) = \left(\frac{\partial\ell(\boldsymbol{\theta})}{\partial\alpha},\frac{\partial\ell(\boldsymbol{\theta})}{\partial\beta},\frac{\partial\ell(\boldsymbol{\theta})}{\partial\phi},\frac{\partial\ell(\boldsymbol{\theta})}{\partial\lambda}\right)^\top.$$

These components are given by

$$\begin{aligned}\frac{\partial\ell(\boldsymbol{\theta})}{\partial\alpha} &= \sum_{i=1}^{n}\log(x_i)-\sum_{i=1}^{n}\log(x_i+1)-\sum_{i=1}^{n}\frac{2\lambda\mathrm{K}(x_i,\alpha,\beta)}{1+\lambda-2\lambda\mathrm{I}_{x_i/(1+x_i)}(\alpha,\beta)}\\ &+(\phi-1)\sum_{i=1}^{n}\frac{\mathrm{K}(x_i,\alpha,\beta)}{\mathrm{I}_{x_i/(1+x_i)}(\alpha,\beta)}-(\phi-1)\sum_{i=1}^{n}\frac{\lambda\mathrm{K}(x_i,\alpha,\beta)}{1+\lambda-\lambda\mathrm{I}_{x_i/(1+x_i)}(\alpha,\beta)},\end{aligned}$$

$$\frac{\partial \ell(\boldsymbol{\theta})}{\partial \beta} = (\phi-1)\sum_{i=1}^{n}\frac{\mathrm{V}(x_i,\alpha,\beta)}{\mathrm{I}_{x_i/(1+x_i)}(\alpha,\beta)} - \sum_{i=1}^{n}\log(x_i+1)$$
$$-\lambda(\phi-1)\sum_{i=1}^{n}\frac{\mathrm{V}(x_i,\alpha,\beta)}{1+\lambda-\lambda\mathrm{I}_{x_i/(1+x_i)}(\alpha,\beta)} - 2\lambda\sum_{i=1}^{n}\frac{\mathrm{V}(x_i,\alpha,\beta)}{1+\lambda-2\lambda\mathrm{I}_{x_i/(1+x_i)}(\alpha,\beta)},$$

$$\frac{\partial \ell(\boldsymbol{\theta})}{\partial \phi} = \frac{n}{\phi} + \sum_{i=1}^{n}\log\left[\mathrm{I}_{x_i/(1+x_i)}(\alpha,\beta)\right] + \sum_{i=1}^{n}\log\left[1+\lambda-\lambda\mathrm{I}_{x_i/(1+x_i)}(\alpha,\beta)\right],$$

$$\frac{\partial \ell(\boldsymbol{\theta})}{\partial \lambda} = \sum_{i=1}^{n}\left[\lambda+\frac{1}{1-2\mathrm{I}_{x_i/(1+x_i)}(\alpha,\beta)}\right]^{-1} + (\phi-1)\sum_{i=1}^{n}\left[\lambda+\frac{1}{1-\mathrm{I}_{x_i/(1+x_i)}(\alpha,\beta)}\right]^{-1},$$

where

$$\mathrm{K}(x_i,\alpha,\beta) = \mathrm{I}_{x_i/(1+x_i)}(\alpha,\beta)[\log(x_i/(1+x_i)+\psi(\alpha+\beta)-\psi(\alpha))] - \frac{\Gamma(\alpha)^2(x_i/(1+x_i))^{\alpha}}{\Gamma(\alpha+1)^2\mathrm{B}(\alpha,\beta)}$$
$$\times\ {}_3\mathrm{F}_2(\alpha,\alpha,1-\beta;\alpha+1,\alpha+1;x_i/(1+x_i)),$$

$$\mathrm{V}(x_i,\alpha,\beta) = \mathrm{I}_{1/(1+x_i)}(\beta,\alpha)[\psi(\beta)-\psi(\alpha+\beta)-\log(1/(1+x_i))] + \frac{(1/(1+x_i))^{\beta}}{\beta^2\mathrm{B}(\alpha,\beta)}$$
$$\times\ {}_3\mathrm{F}_2(1-\alpha,\beta,\beta;\beta+1,\beta+1;1/(1+x_i)),$$

$\psi(z)=\Gamma'(z)/\Gamma(z)$ is the digamma function, $\Gamma(z)$ is the gamma function, and ${}_p\mathrm{F}_q(a;b;z)$ is the generalized hypergeometric function.

The MLEs of $\boldsymbol{\theta}$ are obtained by taking $\mathrm{U}(\boldsymbol{\theta})=\mathbf{0}$, where $\mathbf{0}$ is a null vector of dimension four. The solution cannot be expressed in closed form. However, we can obtain $\hat{\boldsymbol{\theta}}$ using a Broyden–Fletcher–Goldfarb–Shanno (BFGS) optimization algorithm implemented in the R programming language [27].

3. Numerical Results

In this section, synthetic and measured SAR amplitude images corresponding to forest, ocean, and urban regions are modeled by the proposed distribution. Usually, these types of regions are modeled as clutters in target detection and classification problems, which are considered relevant research topics in statistical SAR image processing [28]. All the implementations and numerical experiments are made in R language. The R codes with a function to fit the ET-IB model are available in [29]. In addition, we also provide the pdf, cdf, quantile function, and a function for generating pseudo-random numbers of the ET-IB distribution.

3.1. Analysis with Simulated Data

Monte Carlo simulations are performed to assess the MLE performance for finite signal lengths. We consider the following metrics: mean estimates, bias, standard deviation (SD), and total relative bias (TRB), defined as the sum of the absolute measures of the relative biases. The parameters used for the simulations were defined from the fit of ET-IB distribution in the measured SAR images presented in Section 3.2. Considering three different scenarios with $\boldsymbol{\theta}=(6.3,\,36.2,\,0.4,\,-0.9)^{\top}$, $\boldsymbol{\theta}=(3.0,\,37.5,\,3.7,\,0.8)^{\top}$, and $\boldsymbol{\theta}=(0.4,\,5.3,\,66.9,\,0.9)^{\top}$, we simulate single-look and multi-look SAR amplitude images, related to forest, ocean, and urban regions, respectively. In all scenarios, we simulate 10,000 patches with dimensions 60×60, 90×90, and 120×120 pixels.

The simulation results are summarized in Table 1. As expected, the MLEs converge to the true values of $\boldsymbol{\theta}$, and the bias, the SD, and TRB gradually converge to zero as the image dimensions increase. Notice that the speed of convergence differs among the scenarios. The TRB decays faster in the forest region, which is also the scenario with more accurate estimates (lower relative biases). Meanwhile, the urban region is the one with the slowest convergence. In general, we can see a good performance of the estimators even

in moderate signal lengths, validating the developed estimation theory. It reveals that the ET-IB distribution performs well also for small SAR image patches.

Table 1. Monte Carlo results: mean of maximum likelihood estimates, bias, sd, and TRB.

Scenario				
Forest	$(\alpha, \beta, \phi, \lambda)^\top$		$(6.3, 36.2, 0.4, -0.9)^\top$	
	$n \times n$	60×60	90×90	120×120
	mean	$(6.46, 36.76, 0.40, -0.89)^\top$	$(6.36, 36.40, 0.40, -0.90)^\top$	$(6.33, 36.29, 0.40, -0.90)^\top$
	Bias	$(0.16, 0.53, 0.00, 0.00)^\top$	$(0.06, 0.20, 0.00, 0.00)^\top$	$(0.03, 0.09, 0.00, 0.00)^\top$
	SD	$(0.68, 2.42, 0.06, 0.05)^\top$	$(0.43, 1.56, 0.04, 0.03)^\top$	$(0.35, 1.19, 0.03, 0.05)^\top$
	TRB	0.06	0.02	0.01
Ocean	$(\alpha, \beta, \phi, \lambda)^\top$		$(3.0, 37.5, 3.7, 0.8)^\top$	
	$n \times n$	60×60	90×90	120×120
	mean	$(2.89, 37.28, 4.26, 0.78)^\top$	$(2.94, 37.23, 3.95, 0.79)^\top$	$(2.98, 37.47, 3.81, 0.80)^\top$
	Bias	$(-0.11, -0.22, 0.56, -0.02)^\top$	$(-0.06, -0.27, 0.25, 0.00)^\top$	$(-0.02, -0.03, 0.11, 0.00)^\top$
	SD	$(0.56, 5.66, 1.54, 0.11)^\top$	$(0.39, 4.15, 0.87, 0.07)^\top$	$(0.31, 3.27, 0.59, 0.05)^\top$
	TRB	0.22	0.10	0.04
Urban	$(\alpha, \beta, \phi, \lambda)^\top$		$(0.4, 5.3, 66.9, 0.9)^\top$	
	$n \times n$	60×60	90×90	120×120
	mean	$(0.46, 5.28, 54.04, 0.89)^\top$	$(0.44, 5.29, 59.60, 0.90)^\top$	$(0.43, 5.31, 60.96, 0.90)^\top$
	Bias	$(0.06, -0.02, -12.86, -0.01)^\top$	$(0.04, 0.00, -7.30, 0.00)^\top$	$(0.03, 0.01, -5.94, 0.00)^\top$
	SD	$(0.09, 0.43, 17.31, 0.03)^\top$	$(0.07, 0.29, 17.63, 0.02)^\top$	$(0.06, 0.21, 17.33, 0.02)^\top$
	TRB	0.36	0.21	0.18

3.2. Analysis with SAR Amplitude Data

We used three datasets to assess the performance of the proposed ET-IB distribution in SAR image modeling.

Figure 2a is a single-look amplitude SAR image, with HH polarization, with dimensions of 90×90 pixels, representing a forest region in northern Sweden. This image belongs to a dataset acquired with the CARABAS-II system. The CARABAS-II system is a Swedish ultrawideband (UWB) very-high frequency (VHF) SAR system (for more information, see [30]). Figure 2b,c are four-look SAR images referring to the ocean and urban regions of San Francisco, California, respectively. Figure 2b,c have dimensions of 75×50 pixels and 30×150 pixels. Those images were acquired with the Airborne Synthetic Aperture Radar (AIRSAR) sensor in L-band (see [31] for more information).

Table 2 presents descriptive measures of the considered datasets, such as mean, median, maximum (max.), minimum (min.), coefficients of variation (CV), skewness (CS), and kurtosis (CK). The lower mean and median values in the ocean region may indicate a lower backscatter in the same area. They also present a lower CV. This may be because four looks in the image generation attenuate the noise. The increase in the number of looks tends to mitigate the variability [32]. Furthermore, the high variability of the dataset in the urban region is probably due to the presence of different elements in the scene, such as streets and houses. Finally, the high values of CS and CK of the three datasets are common features in SAR images, since they usually present long and fat tails [33].

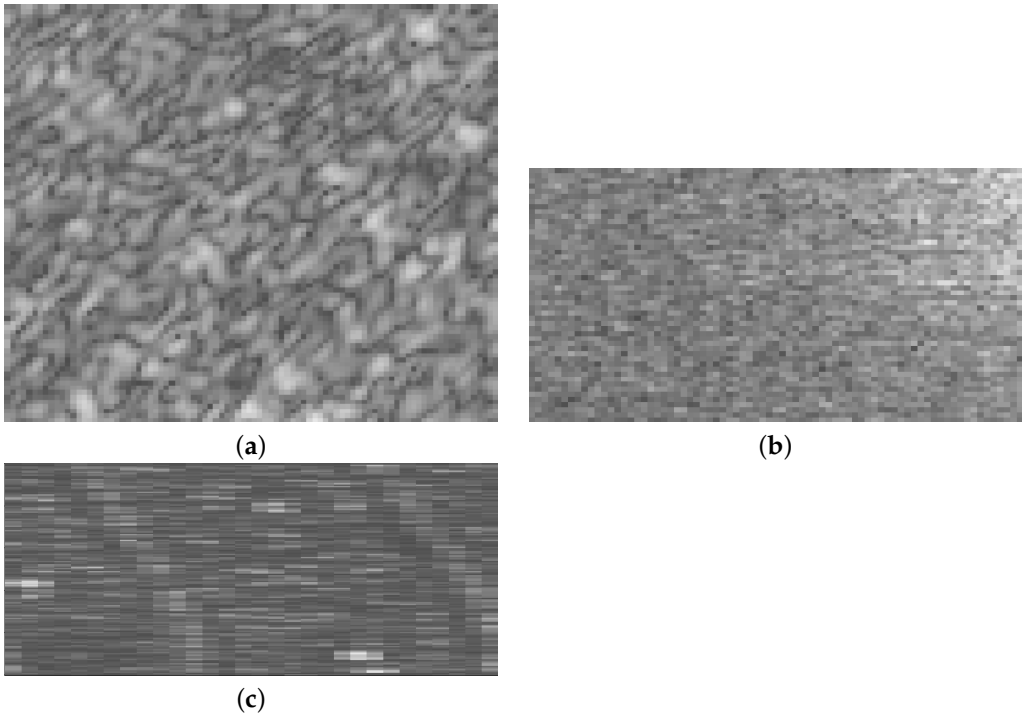


Figure 2. Images used in measured SAR data applications: (**a**) single-look VHF UWB SAR image referring to a forest region in northern Sweden, (**b**,**c**) four-look L-band SAR images referring to the ocean and urban areas, respectively, from San Francisco, California.

Table 2. Summary statistics of datasets.

Dataset	Min.	Max.	Mean	Median	CV(%)	CS	CK
Forest region	7.72×10^{-4}	0.62	0.15	0.14	54.45	0.92	4.32
Ocean region	0.02	0.32	0.10	0.09	41.19	1.47	6.25
Urban region	0.09	3.75	0.45	0.37	68.86	3.21	21.22

For each dataset, we fit the ET-IB distribution and the following competitor models: the IB, Rayleigh, Weibull, log-normal, Rician, K, and $\mathcal{G}_A^0$ distributions. To evaluate and compare the adjustments, we present the number of parameter (NP) and computed the following goodness-of-fit (GoF) statistics: the Akaike Information Criterion (AIC) [34], corrected statistic of Cramér–von Mises (W*), and the Kolmogorov–Smirnov (K-S) test. They are calculated using the *goodness.fit* function from the *AdequacyModel* package [35] in the R statistical computing environment. The distribution with the smallest GoF measures is the one that best fits the dataset. We also presented the p-value of the K-S test, where the null hypothesis is that the sample is drawn from the reference distribution.

Table 3 presents the GoF measures for all fitted models for all types of regions. These measures evidence the superiority of the ET-IB over the classical SAR amplitude image distributions. According to all GoF measures, the best fit is provided by the ET-IB distribution for all three regions. Among the usual distributions, the $\mathcal{G}_A^0$ stood out as the only one besides the ET-IB which did not reject the null hypothesis in the K-S test at 5% of significance level (p-value greater than 0.05). The results highlight the importance of the two additional parameters of the ET-G family for obtaining a distribution with consistently better performance than its baseline in SAR applications.

Table 3. GoF measures for different probability distributions considering the forest, ocean, and urban region datasets. The best results are presented in bold font.

Scenario	Model	NP	AIC	W*	KS (*p*-Value)
Forest	ET-IB	4	**−18,752.34**	**0.028**	**0.005 (0.973)**
	IB	2	−18,468.01	3.923	0.040 (<0.001)
	Rayleigh	1	−18,658.60	0.732	0.021 (<0.001)
	Weibull	2	−18,680.15	0.602	0.017 (0.014)
	Log-normal	2	−17,521.40	15.139	0.108 (<0.001)
	Rician	2	−18,656.60	0.732	0.021 (<0.001)
	K	2	−18,722.74	0.299	0.017 (0.022)
	$\mathcal{G}_A^0$	3	−18,735.88	0.248	0.012 (0.180)
Ocean	ET-IB	4	**−14,354.08**	**0.110**	**0.013 (0.456)**
	IB	2	−14,215.73	2.023	0.047 (<0.001)
	Rayleigh	1	−13,194.10	6.811	0.115 (<0.001)
	Weibull	2	−13,536.55	9.690	0.083 (<0.001)
	Log-normal	2	−14,329.52	0.501	0.843 (<0.001)
	Rician	2	−13,432.68	11.544	0.090 (<0.001)
	K	2	−13,158.91	5.720	0.157 (<0.001)
	$\mathcal{G}_A^0$	3	−14,350.44	0.117	0.015 (0.348)
Urban	ET-IB	4	**−1418.99**	**0.030**	**0.008 (0.927)**
	IB	2	−1072.49	4.301	0.054 (<0.001)
	Rayleigh	1	633.11	22.517	0.161 (<0.001)
	Weibull	2	181.21	17.077	0.105 (<0.001)
	Log-normal	2	312.87	0.381	0.484 (<0.001)
	Rician	2	635.11	22.517	0.161 (<0.001)
	K	2	−321.22	11.406	0.091 (<0.001)
	$\mathcal{G}_A^0$	3	−1406.31	0.092	0.012 (0.543)

Graphical representations of the estimated log-densities of each considered distribution and the log-frequency for each dataset are presented in Figure 3. As expected, the new distribution properly fits the long and fat tails of the three considered datasets. Therefore, the practical importance of the ET-IB distribution as a SAR image descriptor is observed in the current applications. It turned out to be a reliable alternative for modeling pixel amplitude values of single-look and multi-look images characterized as forest, ocean, and urban regions, respectively. In this way, it reveals the potential to compete with the usual distributions to describe these and other types of SAR images, aiming to detect target- and ground-type changes, land classification, etc.

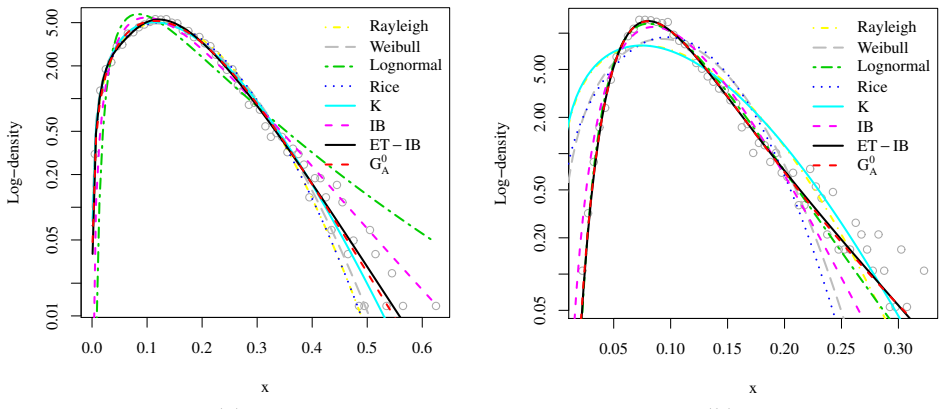
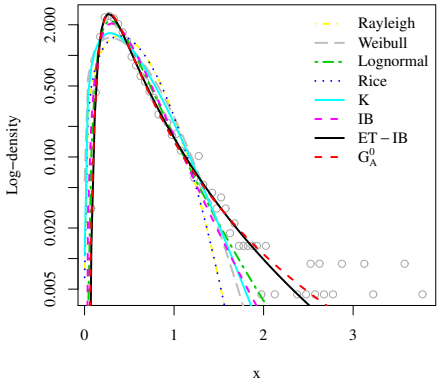


Figure 3. *Cont.*



(**c**)

Figure 3. Log-frequency and estimated log-density of the ET-IB and competitor distributions for (**a**) forest region, (**b**) ocean region, and (**c**) urban region.

4. Conclusions

This paper introduced a new probability density function as a SAR image descriptor named exponentiated transmuted-inverted beta (ET-IB) distribution. We presented important statistical properties of the ET-IB distribution and discussed parameter estimation. The proposed distribution was validated with numerical experiments based on simulated and measured data for modeling forest, ocean, and urban regions in SAR amplitude images. The ET-IB overcomes the baseline distribution in terms of fit performance limitations. Moreover, the proposed ET-IB distribution is adequate for modeling amplitude, single-look, and multi-look data due to the flexibility provided by the additional ET-G family shape parameters. The proposed distribution also works well for the intensity format. Pilot simulations showed that the proposed model outperforms some usual distributions for SAR intensity images according to the GoF measures and log-frequency plot. However, due to simplicity and results similarities, we did not include the results from intensity images in this paper. In summary, the proposed ET-IB distribution showed to be a versatile statistical model for SAR image description. In future works, the ET-IB distribution can serve as an input for several algorithms applicable to SAR image processing, such as regression models, time-series models, and control charts, which useful in several SAR problems such as edge detection, data exploitation, ship detection, segmentation, restoration, pattern recognition, classification, target recognition, change detection, and anomaly detection, as similarly discussed in [2,4,21,30,31,36–42].

Author Contributions: Conceptualization, M.S., R.R.G. and F.M.B.; methodology, M.S., R.R.G., F.M.B. and R.M.; software, M.S., R.R.G., F.M.B. and R.M.; validation, M.S., R.R.G., F.M.B. and R.M.; formal analysis, M.S.; investigation, M.S., R.R.G., F.M.B. and R.M.; resources, M.S., R.R.G., F.M.B. and R.M.; data curation, M.S.; writing—original draft preparation, M.S., R.R.G., F.M.B. and R.M.; writing—review and editing, M.S., R.R.G., F.M.B. and R.M.; visualization, M.S., R.R.G., F.M.B. and R.M.; supervision, R.R.G., F.M.B. and R.M.; project administration, R.R.G., F.M.B. and R.M.; funding acquisition, M.S., R.R.G., F.M.B. and R.M. All authors have read and agreed to the published version of the manuscript.

Funding: This research was partially supported by the Brazilian agencies Coordination for the Improvement of Higher Education Personnel (CAPES), National Council for Scientific and Technological Development (CNPq), and São Paulo Research Foundation (FAPESP) under grant #2020/09838-0 (BI0S—Brazilian Institute of Data Science).

Data Availability Statement: The data are available at https://www.sdms.afrl.af.mil/index.php, accessed on 5 May 2022 and https://ietr-lab.univ-rennes1.fr/polsarpro-bio/san-francisco/, accessed on 5 May 2022.

Conflicts of Interest: The authors declare no conflict of interest.

References

1. Gao, G. Statistical modeling of SAR images: A survey. *Sensors* **2010**, *10*, 775–795. [PubMed]
2. Feng, J.; Cao, Z.; Pi, Y. Multiphase SAR image segmentation with G^0-statistical-model-based active contours. *IEEE Trans. Geosci. Remote Sens.* **2013**, *51*, 4190–4199. [CrossRef]
3. Jain, A.; Singh, D. An optimal selection of probability distribution functions for unsupervised land cover classification of PALSAR-2 data. *Adv. Space Res.* **2018**, *63*, 813–825. [CrossRef]
4. Karine, A.; Toumi, A.; Khenchaf, A.; Hassouni, M.E. Target recognition in Radar images using weighted statistical dictionary-based sparse representation. *IEEE Geosci. Remote Sens. Lett.* **2017**, *14*, 2403–2407. [CrossRef]
5. Nadarajah, S.; Kotz, S. Intensity models for non Rayleigh speckle distributions. *Int. J. Remote Sens.* **2008**, *2*, 529–541.
6. Frery, A.C.; Muller, H.J.; Yanasse, C.C.F.; Sant'Anna, S.J.S. A model for extremely heterogeneous clutter. *IEEE Trans. Geosci. Remote Sens.* **1997**, *35*, 648–659.
7. Cintra, R.J.; Rêgo, L.C.; Cordeiro, G.M.; Nascimento, A.D.C. Beta generalized normal distribution with an application for SAR image processing. *Statistics* **2012**, *2*, 279–294. [CrossRef]
8. Gao, G.; Qin, X.; Zhou, S. Modeling SAR images based on a generalized gamma distribution for texture component. *Prog. Electromagn. Res.* **2013**, *137*, 669–685. [CrossRef]
9. Cordeiro, G.M.; Cintra, R.J.; Rêgo, L.C.; Nascimento, A.D.C. The gamma generalized normal distribution: A descriptor of SAR imagery. *J. Comput. Appl. Math.* **2019**, *347*, 257–272.
10. Vasconcelos, J.M.; Cintra, R.J.; Nascimento, A.D.C.; Rêgo, L.C. The compound truncated Poisson Cauchy model: A descriptor for multimodal data. *J. Comput. Appl. Math.* **2020**, *378*, 112887.
11. Karakus, O.; Kuruoglu, E.E.; Achim, A. A generalized Gaussian extension to the Rician distribution for SAR image modeling. *IEEE Trans. Geosci. Remote Sens.* **2021**, *60*, 5205615. [CrossRef]
12. McDonald, J.B. Some generalized functions for the size distribution of income. *Econometrica* **1984**, *52*, 647–665. [CrossRef]
13. Deng, X.; López-Martínez, C.; Chen, J.; Han, P. Statistical modeling of polarimetric SAR data: A survey and challenges. *Remote Sens.* **2017**, *9*, 348. [CrossRef]
14. MingChun, W.; JiaFeng, Z.; Tao, L. Constant false alarm rate detection method in polarimetric synthetic aperture radar imagery based on whitening filter under inverse beta distribution. *J. Eng.* **2019**, *2019*, 5574–5579. [CrossRef]
15. Merovci, F.; Alizadeh, M.; Yousof, H.M.; Hamedani, G.G. The exponentiated transmuted-G family of distributions: Theory and applications. *Commun. Stat. Theory Methods* **2017**, *46*, 10800–10822. [CrossRef]
16. Okereke, E.W. Exponentiated transmuted Lindley distribution with applications. *Open J. Math. Anal.* **2019**, *3*, 1–18. [CrossRef]
17. Abbas, S.; Mohsin, M.; Pilz, J. A new life time distribution with applications inreliability and environmental sciences. *J. Stat. Manag. Syst.* **2020**, *24*, 453–479.
18. Freitas, C.C.; Frery, A.C.; Correia, A.H. The polarimetric $\mathcal{G}$ distribution for SAR data analysis. *Environmetrics* **2005**, *16*, 13–31. [CrossRef]
19. Guo, R.; Cui, J.; Jing, G.; Zhang, S.; Xing, M. Validating GEV model for reflection symmetry-based ocean ship detection with Gaofen-3 dual-polarimetric data. *Remote Sens.* **2020**, *12*, 1148. [CrossRef]
20. Liao, M.; Wang, C.; Wang, Y.; Jiang, L. Using SAR images to detect ships from sea clutter. *IEEE Geosci. Remote Sens. Lett.* **2008**, *5*, 194–198. [CrossRef]
21. Atteia, G.E.; Collins, M.J. On the use of compact polarimetry SAR for ship detection. *ISPRS J. Photogramm. Remote Sens.* **2012**, *80*, 1–9. [CrossRef]
22. McDonald, J.B.; Xu, Y.J. A generalization of the beta distribution with applications. *J. Econ.* **1995**, *66*, 133–152. [CrossRef]
23. Sagrillo, M.; Guerra, R.R.; Bayer, F.M.; Machado, R. Shiny Application of ET-IB Distribution. Available online: https://estmsp.shinyapps.io/etib/ (accessed on 15 May 2022).
24. Kenney, J.F.; Keeping, E.S. *Mathematics of Statistics*, 3rd ed.; Chapman and Hall Ltd.: London, UK, 1962.
25. Moors, J.J.A. A quantile alternative for kurtosis. *J. R. Stat. Soc. Ser. D Stat.* **1988**, *37*, 25–32. [CrossRef]
26. Pawitan, Y. *In All Likelihood: Statistical Modelling and Inference Using Likelihood*; Oxford University Press: Oxford, UK, 2001.
27. R Core Team. *R: A Language and Environment for Statistical Computing*; R Foundation for Statistical Computing: Vienna, Austria, 2021.
28. Kuttikkad, S.; Chellappa, R. Statistical modeling and analysis of high-resolution Synthetic Aperture Radar images. *Stat. Comput.* **2000**, *10*, 133–145. [CrossRef]
29. Sagrillo, M.; Guerra, R.R.; Bayer, F.M.; Machado, R. R Implementations of ET-IB Distribution. Available online: https://github.com/murilosagrillo/ETIB (accessed on 20 May 2022).
30. Lundberg, M.; Ulander, L.M.H.; Pierson, W.E.; Gustavsson, A. A challenge problem for detection of targets in foliage. In Proceedings of the Defense and Security Symposium, Orlando, FL, USA, 17–21 April 2006; Volume 6237, p. 62370K.
31. Nascimento, A.D.C.; Horta, M.M.; Frery, A.C.; Cintra, R.J. Comparing edge detection methods based on stochastic entropies and distances for PolSAR imagery. *IEEE J. Sel. Top. Appl. Earth Obs. Remote Sens.* **2013**, *7*, 648–663. [CrossRef]
32. Johnsen, H. Multi-look versus single-look processing of synthetic aperture radar images with respect to ocean wavespectra estimation. *Int. J. Remote Sens.* **1992**, *13*, 1627–1643. [CrossRef]
33. Gong, L.; Wang, C.; Wu, F.; Zhang, J.; Zhang, H.; Li, Q. Earthquake-induced building damage detection with post-event sub-meter VHR terra SAR-X staring spotlight imagery. *Remote Sens.* **2016**, *8*, 887. [CrossRef]

34. Akaike, H. A new look at the statistical model identification. *IEEE Trans. Autom. Control* **1974**, *19*, 716–723. [CrossRef]
35. Marinho, P.R.D.; Silva, R.B.; Bourguignon, M.; Cordeiro, G.M.; Nadarajah, S. AdequacyModel: An R package for probability distributions and general purpose optimization. *PLoS ONE* **2019**, *14*, e0221487. [CrossRef]
36. Akbari, V.; Anfinsen, S.N.; Doulgeris, A.P.; Eltoft, T.; Moser, G.; Serpico, S.B. Polarimetric SAR change detection with the complex Hotelling–Lawley Trace Statistic. *IEEE Trans. Geosci. Remote Sens.* **2016**, *64*, 3853–3966. [CrossRef]
37. Yao, J.; Cao, X.; Zhao, Q.; Meng, D.; Xu, Z. Robust subspace clustering via penalized mixture of Gaussians. *Neurocomputing* **2018**, *278*, 4–11. [CrossRef]
38. Yao, J.; Meng, D.; Zhao, Q.; Cao, W.; Xu, Z. Nonconvex-sparsity and Nonlocal-smoothness Based Blind Hyperspectral Unmixing. *IEEE Trans. Image Process.* **2019**, *28*, 2991–3006. [CrossRef] [PubMed]
39. Palm, B.G.; Bayer, F.M.; Cintra, R.J.; Pettersson, M.I.; Machado, R. Rayleigh regression model for ground type detection in SAR imagery. *IEEE Geosci. Remote Sens. Lett.* **2019**, *16*, 1660–1664. [CrossRef]
40. Bayer, D.M.; Bayer, F.M.; Gamba, P. A 3-D spatiotemporal model for remote sensing data cubes. *IEEE Trans. Geosci. Remote Sens.* **2020**, *59*, 1082–1093. [CrossRef]
41. Hong, D.; Gao, L.; Yokoya, N.; Yao, J.; Chanussot, J.; Du, Q.; Zhang, B. More diverse means better: Multimodal deep learning meets remote-sensing imagery classification. *IEEE Trans. Geosci. Remote Sens.* **2020**, *59*, 4340–4354. [CrossRef]
42. Nguyen, H.H.; Cho, S.; Jeong, J.; Choi, M. A D-vine copula quantile regression approach for soil moisture retrieval from dual polarimetric SAR Sentinel-1 over vegetated terrains. *Remote Sens. Environ.* **2021**, *255*, 112283. [CrossRef]